Crystal structure of decoquinate, $C_{24}H_{35}NO_5$

Tawnee M. Ens,[1] James A. Kaduk,[1,2,a)] Megan M. Rost,[3] Anja Dosen,[3] and Thomas N. Blanton[3]
[1]*North Central College, 131 S. Loomis St., Naperville, IL 60540, USA*
[2]*Illinois Institute of Technology, 3101 S. Dearborn St., Chicago, IL 60616, USA*
[3]*ICDD, 12 Campus Blvd., Newtown Square, PA, 19073-3273, USA*

(Received 20 June 2024; accepted 10 September 2024)

The crystal structure of decoquinate has been solved and refined using synchrotron X-ray powder diffraction data and optimized using density functional theory techniques. Decoquinate crystallizes in space group $P2_1/n$ (#14) with $a = 46.8261(5)$, $b = 12.94937(12)$, $c = 7.65745(10)$ Å, $\beta = 91.972(1)$, $V = 4640.48(7)$ Å^3, and $Z = 8$ at 295 K. The crystal structure consists of alternating layers of hydrocarbon chains and ring systems along the *a*-axis. Hydrogen bonds link the ring systems along the *b*-axis. The rings stack along the *c*-axis. The two independent decoquinate molecules have very different conformations, one of which is typical and the other has an unusual orientation of the decyl chain with respect to the hydroxyquinoline ring system, facilitating chain packing. The powder pattern has been submitted to the ICDD for inclusion in the Powder Diffraction File™ (PDF®).

[doi:10.1017/S0885715624000502]

Key words: decoquinate, Deccox®, crystal structure, Rietveld refinement, density functional theory

I. INTRODUCTION

Decoquinate (marketed under the trade names Deccox and Decoxy) was approved by the FDA in 2004 for animal feed use and shows antimicrobial and antiparasitic properties as a veterinary medication (https://www.accessdata.fda.gov/scripts/cdrh/cfdocs/cfcfr/CFRSearch.cfm?fr=558.195; Souza et al., 2022). Decoquinate is used primarily to treat coccidiosis caused by parasites including *Eimeria* and Toxoplasmosis caused by *Toxoplasma* in some domestic animals. Though most often connected with animals, coccidiosis can occur in humans, particularly through contact with domestic dogs and cats. When infected with these parasitic infections, the primary symptom is diarrhea. However, in some cases, the infection can lead to miscarriage and abortion of embryos. To combat diarrhea in young animals, decoquinate can be administered in the early stages to be effective against infection (Taylor and Bartram, 2012). The systematic name (CAS Registry Number 18507-89-6) is ethyl 6-(decyloxy)-7-ethoxy-4-hydroxyquinoline-3-carboxylate. A two-dimensional molecular diagram of decoquinate is shown in Figure 1.

International Patent Application WO 2020/140197 A1 (Wang et al., 2020) claims decoquinate compositions prepared by hot-melt extrusion for use against malaria parasites. The application also contains X-ray powder data for pure decoquinate active pharmaceutical ingredient; however, no crystal structure is reported.

This work was carried out as part of a project (Kaduk et al., 2014) to determine the crystal structures of large-volume commercial pharmaceuticals and include high-quality powder diffraction data for them in the Powder Diffraction File (Kabekkodu et al., 2024).

II. EXPERIMENTAL

Decoquinate was a commercial reagent, purchased from TargetMol (Batch #113288), and was used as-received. The white powder was packed into a 1.5 mm diameter Kapton capillary and rotated during the measurement at ~50 Hz. The powder pattern was measured at 295 K at beamline 11-BM (Antao et al., 2008; Lee et al., 2008; Wang et al., 2008) of the Advanced Photon Source at Argonne National Laboratory using a wavelength of 0.45808(2) Å from 0.5 to 50° 2θ with a step size of 0.001° and a counting time of 0.1 s/step. The high-resolution powder diffraction data were collected using 12 silicon crystal analyzers that allow for high angular resolution, high precision, and accurate peak positions. A mixture of silicon (NIST SRM 640c) and alumina (NIST SRM 676a) standards (ratio Al_2O_3:Si = 2:1 by weight) was used to calibrate the instrument and refine the monochromatic wavelength used in the experiment.

The pattern was difficult to index. The long 46 Å axis means that most of the low-angle peaks are of the form *h00* and *hk0*, and it was difficult to define the short axis. After several attempts (with smaller *c*-axes), the pattern was indexed using JADE Pro (MDI, 2024) on a primitive monoclinic unit cell with $a = 46.77298$, $b = 12.95209$, $c = 7.65585$ Å, $\beta = 91.97°$, $V = 4635.24$ Å^3, and $Z = 8$. The suggested space group was $P2_1/n$, which was confirmed by the successful solution and refinement of the structure. A reduced cell search of

a)Author to whom correspondence should be addressed. Electronic mail: kaduk@polycrystallography.com

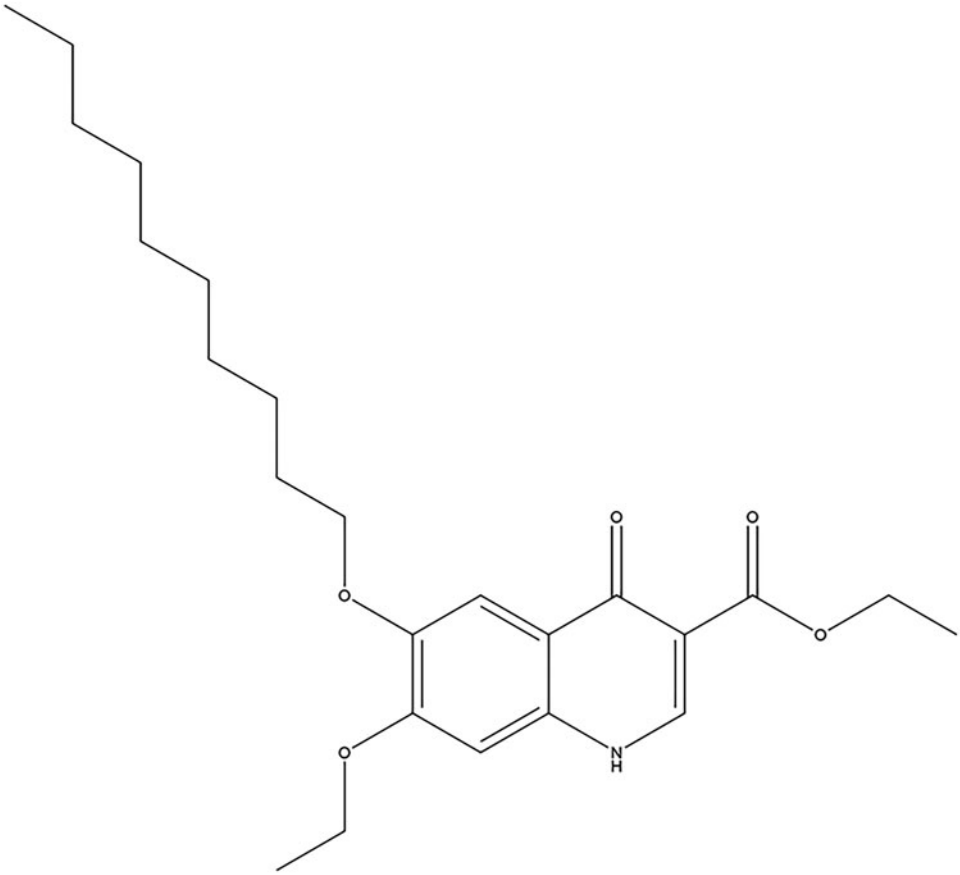

Figure 1. The two-dimensional structure of decoquinate.

the Cambridge Structural Database (Groom et al., 2016) yielded 19 hits but no decoquinate derivatives.

The decoquinate molecule was downloaded from PubChem (Kim et al., 2023) as Conformer3D_CID_29112.sdf. The downloaded conformation turns out to be similar to that of molecule 2. It was converted to a *.mol2 file using Mercury (Macrae et al., 2020). The crystal structure was solved using Monte Carlo simulated annealing techniques

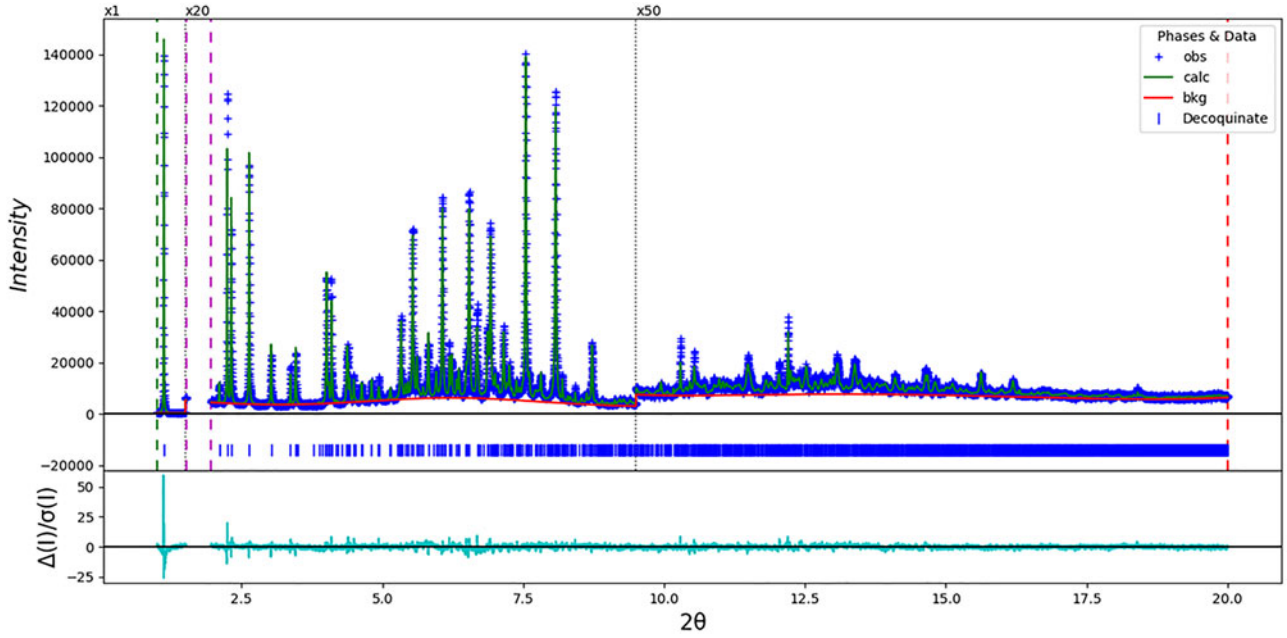

Figure 2. The Rietveld plot for the refinement of decoquinate. The blue crosses represent the observed data points, and the green line is the calculated pattern. The cyan curve is the normalized error plot, and the red line is the background curve. The vertical scale has been multiplied by a factor of 20× for $2\theta > 1.5°$ 50× for $2\theta > 9.0°$.

https://doi.org/10.1017/S0885715624000502 Published online by Cambridge University Press

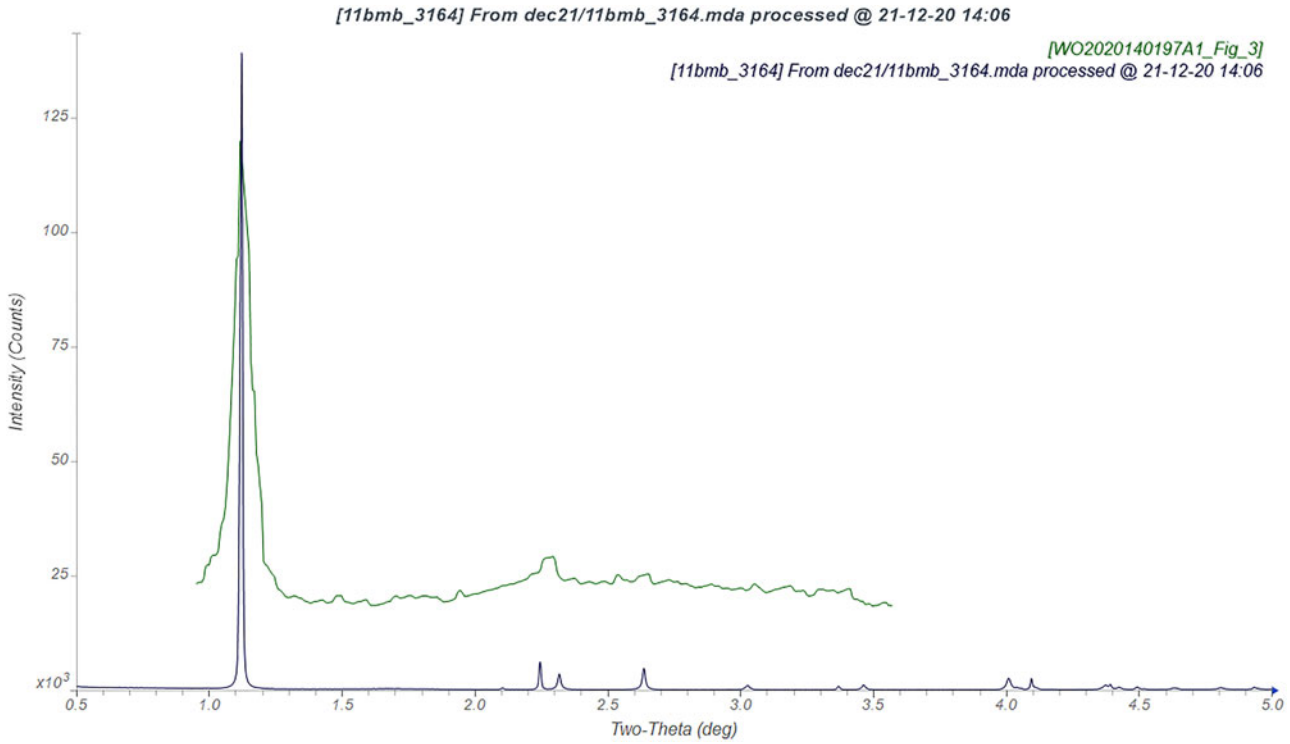

Figure 3. Comparison of the synchrotron pattern from this study of decoquinate (black) to that reported by Wang et al. (2020; green). The Wang et al. pattern (measured using Cu K_α radiation) was digitized using UN-SCAN-IT (Silk Scientific, 2013) and converted to the synchrotron wavelength of 0.458208(2) Å using JADE Pro (MDI, 2024). Image generated using JADE Pro (MDI, 2024).

as implemented in EXPO2014 (Altomare et al., 2013) using two decoquinate molecules as fragments. The torsion angles of the decyl side chains were fixed at approximately 180°. One of the ten solutions had a figure of merit much better than the others.

Rietveld refinement was carried out with GSAS-II (Toby and Von Dreele, 2013). Only the 1.0–20.0° portion of the pattern was included in the refinements ($d_{\min}$ = 1.319 Å). The region 1.51–1.96° 2θ, which contains a peak from the Kapton capillary, was excluded from the refinement. All non-H-bond distances and angles were subjected to restraints based on a Mercury/Mogul Geometry Check (Bruno et al., 2004; Sykes et al., 2011). The Mogul average and standard deviation for each quantity were used as the restraint parameters. The hydroxyquinoline rings were restrained to be planar. The hydrogen atoms were included in calculated positions, which were recalculated during the refinement using Materials Studio (Dassault Systèmes, 2023). The U_{iso} of the heavy atoms were grouped by chemical similarity. The U_{iso} for the H atoms were fixed at 1.3× the U_{iso} of the heavy atoms to which they are attached. The peak profiles were described using the generalized microstrain model

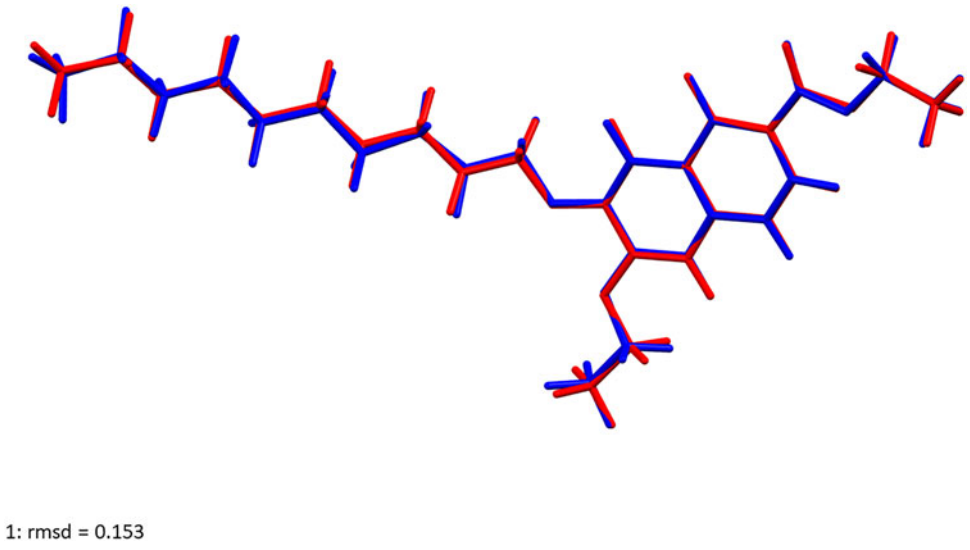

Figure 4. Comparison of the Rietveld-refined (red) and VASP-optimized (blue) structures of decoquinate molecule 1. The root-mean-square Cartesian displacement is 0.153 Å. Image generated using Mercury (Macrae et al., 2020).

https://doi.org/10.1017/S0885715624000502 Published online by Cambridge University Press

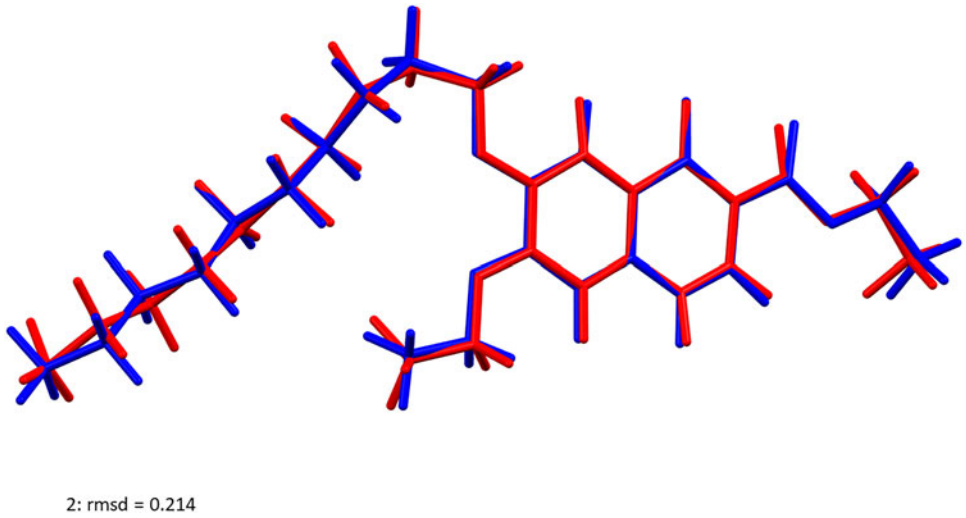

Figure 5. Comparison of the Rietveld-refined (red) and VASP-optimized (blue) structures of decoquinate molecule 2. The root-mean-square Cartesian displacement is 0.214 Å. Image generated using Mercury (Macrae et al., 2020).

(Stephens, 1999). The background was modeled using a 6-term shifted Chebyshev polynomial, with a peak at 6.18° to model the scattering from the Kapton capillary and an amorphous component.

The final refinement of 216 variables using 18,586 observations and 142 restraints yielded the residuals $R_{wp} = 0.1060$ and goodness of fit = 2.02. The largest peak (1.18 Å from C92) and hole (1.57 Å from O69) in the difference Fourier map were 0.17(4) and −0.17(4) eÅ^{-3}, respectively. The final Rietveld plot is shown in Figure 2. The largest features in the normalized error plot are in the shape of the lowest-angle 200 peak.

The crystal structure of decoquinate was optimized (fixed experimental unit cell) with density functional techniques using VASP (Kresse and Furthmüller, 1996) through the MedeA graphical interface (Materials Design, 2024). The calculation was carried out on 32 cores of a 144-core (768 Gb memory) HPE Superdome Flex 280 Linux server at North Central College. The calculation used the GGA-PBE functional, a plane-wave cutoff energy of 400.0 eV, and a k-point spacing of 0.5 Å^{-1} leading to a 2 × 1 × 1 mesh and took ∼126 h. Single-point density functional calculations (fixed experimental cell) and population analysis were carried out using CRYSTAL23 (Erba et al., 2023). The basis sets for the H, C, N, and O atoms in the calculation were those of Gatti et al. (1994). The calculations were run on a 3.5 GHz PC using 8 k-points and the B3LYP functional and took ∼11 h.

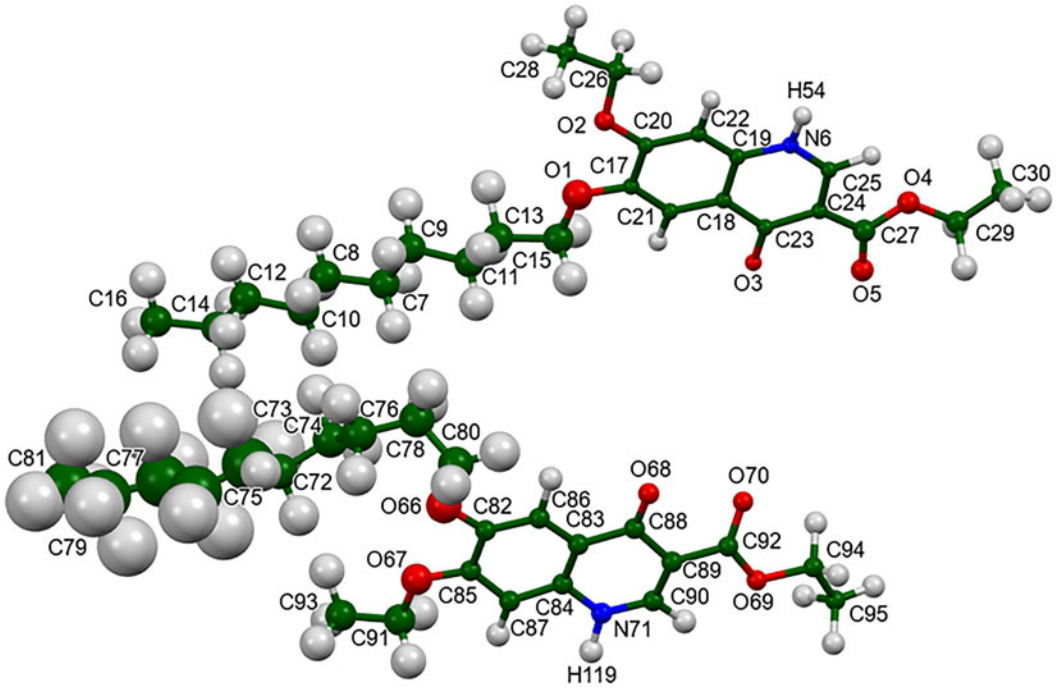

Figure 6. The asymmetric unit of decoquinate, with the atom numbering. The atoms are represented by 50% probability spheroids. Image generated using Mercury (Macrae et al., 2020).

https://doi.org/10.1017/S0885715624000502 Published online by Cambridge University Press

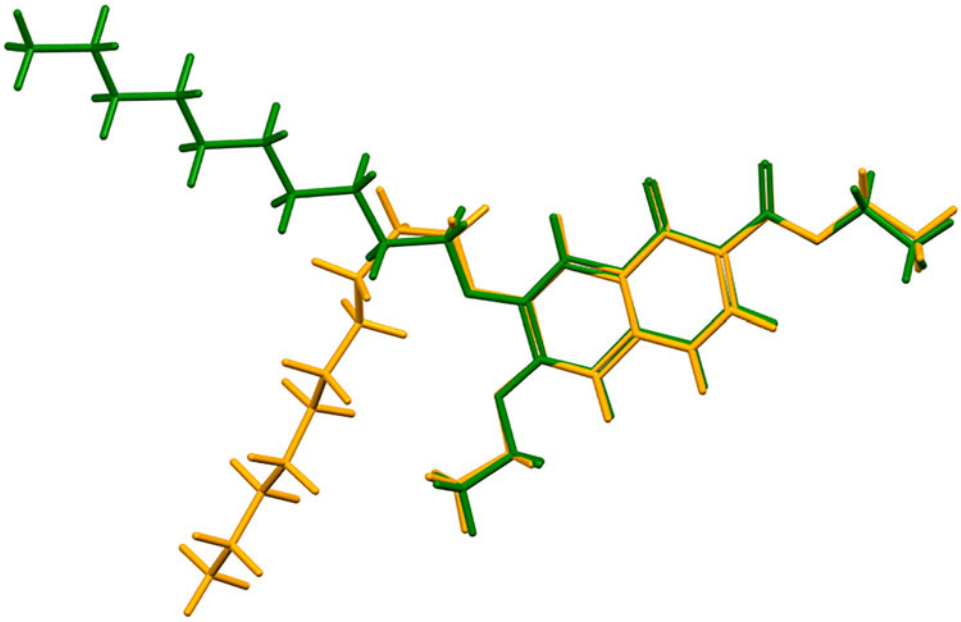

Figure 7. Comparison of decoquinate molecule 1 (green) and molecule 2 (orange). Image generated using Mercury (Macrae et al., 2020).

III. RESULTS AND DISCUSSION

The powder pattern of this study is similar enough to that reported by Wang et al. (2020) to suggest that they probably represent the same material (Figure 3). Wang's pattern is limited and of low quality, so the conclusion is tentative.

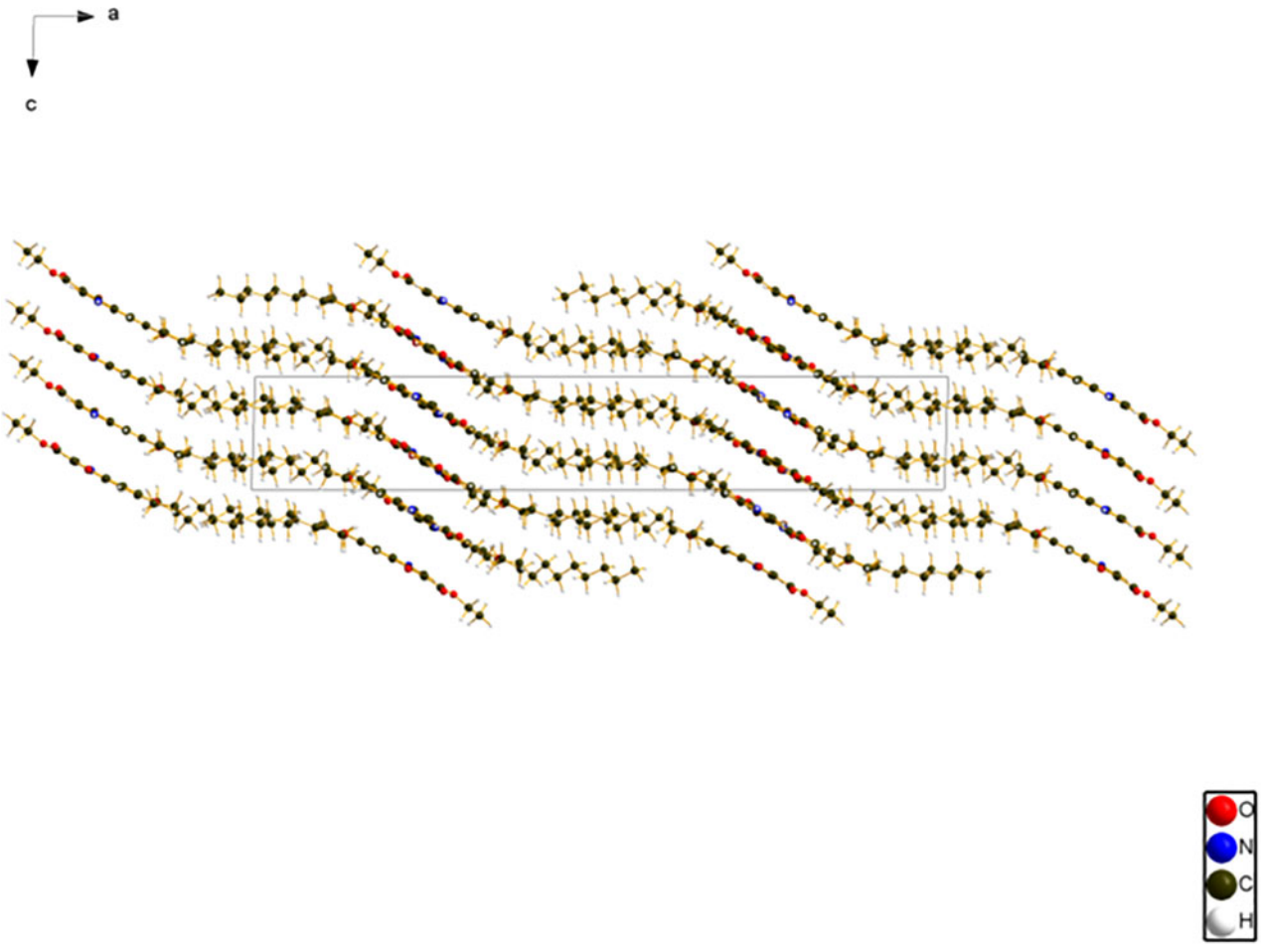

Figure 8. The crystal structure of decoquinate is viewed down the *b*-axis. Image generated using Diamond (Crystal Impact, 2023).

https://doi.org/10.1017/S0885715624000502 Published online by Cambridge University Press

TABLE I. Hydrogen bonds (CRYSTAL23) in decoquinate.

H-bond	D–H (Å)	H···A (Å)	D···A (Å)	D–H···A (Å)	Overlap (e)	*E* (kcal/mol)
N6–H54···O5	1.041	1.816	2.798	155.9	0.052	5.3
N71–H119···O70	1.040	1.911	2.866	151.0	0.044	4.8
C21–H52···O3	1.091	2.476[a]	2.834	97.6	0.021	
C22–H53···O5	1.088	2.266	3.148	136.7	0.024	
C25–H55···O4	1.088	2.287[a]	2.635	96.1	0.014	
C25–H55···O3	1.088	2.347	3.136	128.0	0.017	
C86–H117···O68	1.091	2.414[a]	2.795	98.7	0.023	
C87–H118···O70	1.089	2.208	3.108	138.5	0.026	
C90–H120···O68	1.088	2.337	3.058	122.1	0.016	
C93–H123···O2	1.099	2.786	3.745	149.6	0.010	

[a]Intramolecular.

The root-mean-square Cartesian displacement of the non-H atoms in the Rietveld-refined and VASP-optimized molecules is 0.153 Å for molecule 1 (Figure 4) and 0.214 Å for molecule 2 (Figure 5). The agreement is within the normal range for correct structures (van de Streek and Neumann, 2014). The asymmetric unit with the atom numbering is presented in Figure 6. The displacement parameters for the decyl chain in molecule 2 are larger than those of the other atoms. The remainder of this discussion will emphasize the VASP-optimized structure.

The two independent decoquinate molecules have very different conformations (Figure 7). While the cores of the molecules are very similar, they differ in the orientation of the decyl group. All of the bond distances, bond angles, and most of the torsion angles fall within the normal ranges indicated by a Mercury Mogul Geometry check (Macrae et al., 2020). Only the C74–C76–C78–C80 (−96°) and O66–C80–C78–C76 (38°) torsion angles are flagged as unusual. Both of these lie on the tails of minor *gauche* populations of mainly *trans* torsion angles. These torsion angles reflect the orientation of the decyl chain with respect to the hydroxyquinoline ring system. Visually this looks unusual, compared to the more-normal orientation of molecule 1. Molecule 2 is unusual, presumably to yield better packing of the chains in the solid state.

Quantum chemical geometry optimization of the isolated molecules (DFT/B3LYP/6-31G*/water) using Spartan ‘20 (Wavefunction, 2020) indicated that molecule 2 is higher in energy than molecule 1 by 1.2 kcal/mol. The energies are thus very close, despite the different conformations. The global minimum-energy conformation (molecular mechanics force field) folds on itself to make the chain and ring system parallel. Solid-state interactions are thus important in determining the observed conformations.

The crystal structure consists of alternating layers of hydrocarbon chains and ring systems along the *a*-axis (Figure 8). Hydrogen bonds (discussed below) link the ring systems along the *b*-axis. The rings stack along the *c*-axis. The mean planes of both hydroxyquinoline ring systems are approximately −3,0,1. The distances between the centroids of the ring systems are 4.786 and 5.566 Å.

Analysis of the contributions to the total crystal energy of the structure using the Forcite module of Materials Studio (Dassault Systèmes, 2023) indicates that bond distance, bond angle, and torsion angle distortion terms contribute significantly to the intramolecular energy. The intermolecular

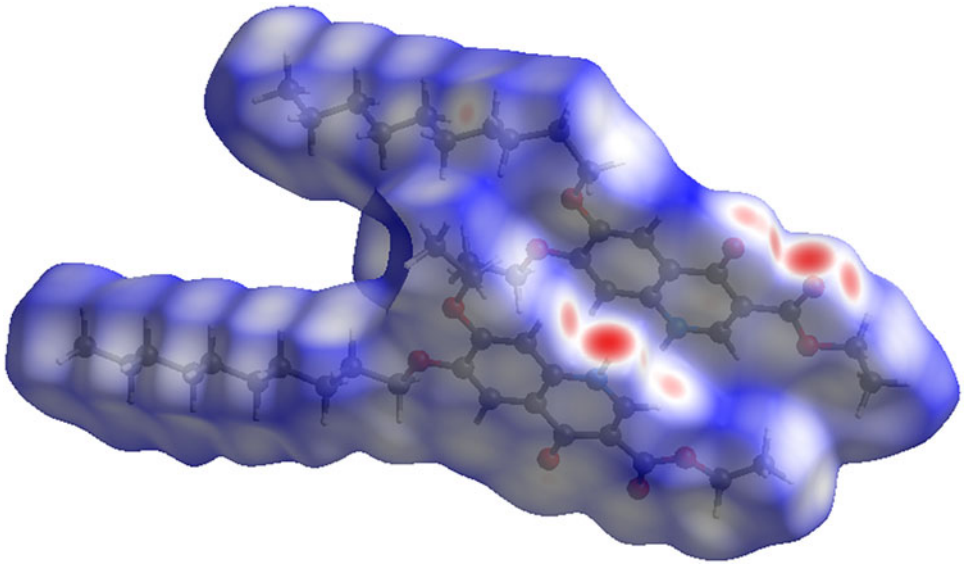

Figure 9. The Hirshfeld surface of decoquinate. Intermolecular contacts longer than the sums of the van der Waals radii are colored blue, and contacts shorter than the sums of the radii are colored red. Contacts equal to the sums of radii are white. Image generated using CrystalExplorer (Spackman et al., 2021).

https://doi.org/10.1017/S0885715624000502 Published online by Cambridge University Press

energy is dominated by van der Waals and electrostatic attractions, which, in this force field analysis, also include hydrogen bonds. The hydrogen bonds are better analyzed using the results of the DFT calculations.

Only two classical hydrogen bonds are present in the crystal structure (Table I). Both N6–H54···O5 and N71–H119···O70 hydrogen bonds link the ring systems along the *b*-axis. The graph set (Etter, 1990; Bernstein et al., 1995; Motherwell et al., 2000) of each is *C1,1(6)*. The energies of the N–H–O hydrogen bonds were calculated using the correlation of Wheatley and Kaduk (2019). Several C–H···O hydrogen bonds link the ring systems, and one methyl group of an ethoxyl group participates in a C–H···O hydrogen bond.

The volume enclosed by the Hirshfeld surface of decoquinate (Figure 9, Hirshfeld, 1977; Spackman et al., 2021) is 1146.54 Å^3, which constitutes 98.83% of the unit cell volume. The packing density is thus fairly typical. The only significant close contacts (red in Figure 9) involve the hydrogen bonds. The volume/non-hydrogen atom is larger than normal, measuring 19.3 Å^3.

The Bravais-Friedel-Donnay-Harker (Bravais, 1866; Friedel, 1907; Donnay and Harker, 1937) morphology suggests that we might expect platy morphology for decoquinate, with {200} as the major faces. A second-order spherical harmonic model was included in the refinement. The texture index was 1.006, indicating that the preferred orientation was not significant in this rotated capillary specimen.

IV. DEPOSITED DATA

The powder pattern of decoquinate from this synchrotron data set has been submitted to the ICDD for inclusion in the Powder Diffraction File. The Crystallographic Information Framework (CIF) files containing the results of the Rietveld refinement (including the raw data) and the DFT geometry optimization were deposited with the ICDD. The data can be requested at pdj@icdd.com.

Acknowledgements

The use of the Advanced Photon Source at Argonne National Laboratory was supported by the U.S. Department of Energy, Office of Science, Office of Basic Energy Sciences, under Contract No. DE-AC02-06CH11357. This work was partially supported by the International Centre for Diffraction Data. We thank Saul Lapidus for his assistance in the data collection.

Conflicts of interest

The authors have no conflicts of interest to declare.

REFERENCES

Altomare, A., C. Cuocci, C. Giacovazzo, A. Moliterni, R. Rizzi, N. Corriero, and A. Falcicchio. 2013. "EXPO2013: A Kit of Tools for Phasing Crystal Structures from Powder Data." *Journal of Applied Crystallography* 46: 1231–5.

Antao, S. M., I. Hassan, J. Wang, P. L. Lee, and B. H. Toby. 2008. "State-of-the-Art High-Resolution Powder X-ray Diffraction (HRPXRD) Illustrated with Rietveld Refinement of Quartz, Sodalite, Tremolite, and Meionite." *Canadian Mineralogist* 46: 1501–9.

Bernstein, J., R. E. Davis, L. Shimoni, and N. L. Chang. 1995. "Patterns in Hydrogen Bonding: Functionality and Graph Set Analysis in Crystals." *Angewandte Chemie International Edition in English* 34: 1555–73.

Bravais, A. 1866. *Etudes Cristallographiques*. Paris, Gauthier Villars.

Bruno, I. J., J. C. Cole, M. Kessler, J. Luo, W. D. S. Motherwell, L. H. Purkis, B. R. Smith, R. Taylor, R. I. Cooper, S. E. Harris, and A. G. Orpen. 2004. "Retrieval of Crystallographically-Derived Molecular Geometry Information." *Journal of Chemical Information and Computer Sciences* 44: 2133–44.

Crystal Impact. 2023. *Diamond V. 5.0.0*. Bonn: Crystal Impact - Dr. H. Putz & Dr. K. Brandenburg. Windows.

Dassault Systèmes. 2023. *BIOVIA Materials Studio 2024*. San Diego, CA, BIOVIA.

Donnay, J. D. H., and D. Harker. 1937. "A New Law of Crystal Morphology Extending the Law of Bravais." *American Mineralogist* 22: 446–67.

Erba, A., J. K. Desmarais, S. Casassa, B. Civalleri, L. Donà, I. J. Bush, B. Searle, L. Maschio, L.-E. Daga, A. Cossard, C. Ribaldone, E. Ascrizzi, N. L. Marana, J.-P. Flament, and B. Kirtman. 2023. "CRYSTAL23: A Program for Computational Solid State Physics and Chemistry." *Journal of Chemical Theory and Computation* 19: 6891–932. doi:10.1021/acs.jctc.2c00958.

Etter, M. C. 1990. "Encoding and Decoding Hydrogen-Bond Patterns of Organic Compounds." *Accounts of Chemical Research* 23: 120–6.

Friedel, G. 1907. "Etudes sur la loi de Bravais." *Bulletin de la Société Française de Minéralogie* 30: 326–455.

Gatti, C., V. R. Saunders, and C. Roetti. 1994. "Crystal-Field Effects on the Topological Properties of the Electron-Density in Molecular Crystals – the Case of Urea." *Journal of Chemical Physics* 101: 10686–96.

Groom, C. R., I. J. Bruno, M. P. Lightfoot, and S. C. Ward. 2016. "The Cambridge Structural Database." *Acta Crystallographica Section B: Structural Science, Crystal Engineering and Materials* 72: 171–9.

Hirshfeld, F. L. 1977. "Bonded-Atom Fragments for Describing Molecular Charge Densities." *Theoretica Chemica Acta* 44: 129–38.

Kabekkodu, S., A. Dosen, and T. N. Blanton. 2024. "PDF-5+: A Comprehensive Powder Diffraction File™ for Materials Characterization." *Powder Diffraction* 39: 47–59.

Kaduk, J. A., C. E. Crowder, K. Zhong, T. G. Fawcett, and M. R. Suchomel. 2014. "Crystal Structure of Atomoxetine Hydrochloride (Strattera), $C_{17}H_{22}NOCl$." *Powder Diffraction* 29: 269–73.

Kim, S., J. Chen, T. Cheng, A. Gindulyte, J. He, S. He, Q. Li, B. A. Shoemaker, P. A. Thiessen, B. Yu, L. Zaslavsky, J. Zhang, and E. E. Bolton. 2023. "Pubchem 2023 Update." *Nucleic Acids Research* 51 (D1): D1373–80. doi:10.1093/nar/gkac956.

Kresse, G., and J. Furthmüller. 1996. "Efficiency of Ab-Initio Total Energy Calculations for Metals and Semiconductors Using a Plane-Wave Basis Set." *Computational Materials Science* 6: 15–50.

Lee, P. L., D. Shu, M. Ramanathan, C. Preissner, J. Wang, M. A. Beno, R. B. Von Dreele, L. Ribaud, C. Kurtz, S. M. Antao, X. Jiao, and B. H. Toby. 2008. "A Twelve-Analyzer Detector System for High-Resolution Powder Diffraction." *Journal of Synchrotron Radiation* 15: 427–32.

Macrae, C. F., I. Sovago, S. J. Cottrell, P. T. A. Galek, P. McCabe, E. Pidcock, M. Platings, G. P. Shields, J. S. Stevens, M. Towler, and P. A. Wood. 2020. "Mercury 4.0: From Visualization to Design and Prediction." *Journal of Applied Crystallography* 53: 226–35.

Materials Design. 2024. *MedeA 3.7.2*. San Diego, CA, Materials Design Inc.

MDI. 2024. *JADE Pro Version 9.0*. Livermore, CA, Materials Data.

Motherwell, W. D. S., G. P. Shields, and F. H. Allen. 2000. "Graph-Set and Packing Analysis of Hydrogen-Bonded Networks in Polyamide Structures in the Cambridge Structural Database." *Acta Crystallographica B* 56: 857–71.

Silk Scientific. 2013. *UN-SCAN-IT 7.0*. Orem, UT, Silk Scientific Corporation.

Souza, T. S., D. R. M. Moreira, and H. R. Marcelino. 2022. "Chemical and Pharmacological Properties of Decoquinate: A Review of Its Pharmaceutical Potential and Future Perspectives." *Pharmaceutics* 14: 1383. doi:10.3390/pharmaceutics14071383

Spackman, P. R., M. J. Turner, J. J. McKinnon, S. K. Wolff, D. J. Grimwood, D. Jayatilaka, and M. A. Spackman. 2021. "Crystalexplorer: A Program for Hirshfeld Surface Analysis, Visualization and Quantitative Analysis

of Molecular Crystals." *Journal of Applied Crystallography* 54: 1006–11. doi:10.1107/S1600576721002910

Stephens, P. W. 1999. "Phenomenological Model of Anisotropic Peak Broadening in Powder Diffraction." *Journal of Applied Crystallography* 32: 281–9.

Sykes, R. A., P. McCabe, F. H. Allen, G. M. Battle, I. J. Bruno, and P. A. Wood. 2011. "New Software for Statistical Analysis of Cambridge Structural Database Data." *Journal of Applied Crystallography* 44: 882–6.

Taylor, M. A., and D. J. Bartram. 2012. "The History of Decoquinate in the Control of Coccidial Infections in Ruminants." *Journal of Veterinary Pharmacology and Therapeutics* 35: 417–27. doi:10.1111/j.1365-2885.2012.01421.x.

Toby, B. H., and R. B. Von Dreele. 2013. "GSAS II: The Genesis of a Modern Open Source All Purpose Crystallography Software Package." *Journal of Applied Crystallography* 46: 544–9.

van de Streek, J., and M. A. Neumann. 2014. "Validation of molecular crystal structures from Powder Diffraction Data with Dispersion-Corrected Density Functional Theory (DFT-D)." *Acta Crystallographica Section B: Structural Science, Crystal Engineering and Materials* 70: 1020–32.

Wang, J., B. H. Toby, P. L. Lee, L. Ribaud, S. M. Antao, C. Kurtz, M. Ramanathan, R. B. Von Dreele, and M. A. Beno. 2008. "A Dedicated Powder Diffraction Beamline at the Advanced Photon Source: Commissioning and Early Operational Results." *Review of Scientific Instruments* 79: 085105.

Wang, H., S. Liang, Y. Fan, Z. Huang, S. Zhao, L. Qin, and X. Chen. 2020. "Nanoparticle Formulations of Decoquinate in the Form of Solid Solution." International Patent Application WO 2020/140197 A1.

Wavefunction, Inc. 2020. *Spartan '20. V. 1.0.0*. Irvine, CA: Wavefunction Inc.

Wheatley, A. M., and J. A. Kaduk. 2019. "Crystal Structures of Ammonium Citrates." *Powder Diffraction* 34: 35–43.